applied optics

Three-degrees-of-freedom laser interferometer based on differential wavefront sensing with wide angular measurement range

Fuzhong Yang,[1,2] Ming Zhang,[1,2,*] Weinan Ye,[1,2] and Leijie Wang[1,2]

[1]State Key Laboratory of Tribology, Department of Mechanical Engineering, Tsinghua University, Beijing 100084, China
[2]Beijing Lab of Precision/Ultra-Precision Manufacture Equipment and Control, Tsinghua University, Beijing 100084, China
*Corresponding author: zm01@mails.tsinghua.edu.cn

We present a three-degrees-of-freedom laser interferometer based on differential wavefront sensing with a wide angular measurement range. To obtain measurement signals with a high AC/DC ratio and improve the linearity of differential wavefront sensing in a wide range angular displacement measurement, a fiber bundle instead of a quadrant photodiode is applied to receive the interference light. Meanwhile, a decoupled algorithm with quadratic correction derived by the ray tracing method and kinematic analysis is detailed in the case of the wide range angular displacement. The simulation and experimental results prove that the laser interferometer with the proposed structure could realize hundreds of microradian range of angular displacement measurement, which are expanded in the differential wavefront sensing.   © 2019 Optical Society of America

https://doi.org/10.1364/AO.58.000723

1. INTRODUCTION

Optical interferometry methods have been widely used in high-precision multidegree-of-freedom measurement systems [1–3]. In contrast to the combination of multiple laser interferometers, differential wavefront sensing (DWS) is a relatively new method of simultaneous linear and angular displacement measurement [4–13]. It can also be adopted in the application of optical alignment with microradian absolute accuracy [14–16]. In the laser interferometer space antenna (LISA) project, a three-degrees-of-freedom (DoFs) metrology based on DWS was first developed [3,4]. However, owing to the unparalleled interference beams in the angular displacement, fringes emerge in the interference area and the fringe period decreases as the angle between the two interference beams enlarges. Thus, the AC/DC ratio of each measurement signal will drop down [3,9]. Given the total input power of photodetector fixed in the actual metrology, the AC amplitude is influenced by the AC/DC ratio of interference signals. Lower AC amplitude leads to higher electronic noise, and even a measurement failure. Consequently, the linear rotational measurement range of DWS with the quadrant photodiode (QPD) is limited to tens of microradians [12,13]. For accurate rotational measurement, many analytical models have been proposed for the DWS technique, mainly concentrating on the prediction of scaling factors [8,9] and the nonlinearity of DWS detection [3,10]. On the other side, the relation between the measurement phase and

multidegree-of-freedom displacement as well as the decoupled algorithm in DWS is not derived and illustrated in detail. Considering the tilt-to-length coupling, a displacement measurement error would be tens of nanometers with the decoupled method before, and quadratic correction is effective to diminish this error [17].

In this paper, a laser interferometer based on DWS that employs a fiber bundle as the receiver of the interference light is proposed to realize simultaneous measurement of three DoFs with a wide angular measurement range. The simulation results prove that the interferometer can maintain a high AC/DC ratio and linearity across a wide angular measurement range and the decoupled algorithm derived from the relation between the three DoFs displacement and measurement phases can effectively minimize the tilt-to-length coupling to sub-nanometers in the ±534 μrad rotational range. Finally, it has been tested through experiments with a contrast device.

2. STRUCTURE AND METHOD

Figure 1(a) shows the schematic of the laser interferometer proposed for measurement of three DoFs with wide angular measurement range. Compared to the interferometer using DWS before, the main difference in optical structure is that a fiber bundle and four photodetectors are used to receive the interference light instead of a QPD. After the laser emitted from the laser source goes through the interferometer, four interference
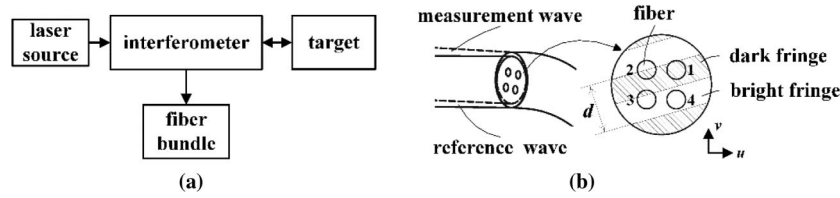
Fig. 1. (a) Schematic of interferometer for measurement of three DoFs in a wide range rotation. (b) The fiber bundle surface structure (exaggerated to be clear).

signals are obtained by the fiber bundle without a fiber coupler, transferred to the photodetectors, and converted to phase information. Figure 1(b) shows the fiber bundle surface structure, which consists of four individual multimode optical fibers, on which the fringes are revealed where an angle exists between two interference beams.

Not taking into account any error, the light intensity of the optical interference signal obtained by each fiber in the bundle can be expressed as

$$I = \iint_D I(u,v)\mathrm{d}u\mathrm{d}v = I_{\mathrm{DC}} + I_{\mathrm{AC}}, \tag{1}$$

where I_{DC} and I_{AC} are the light intensity of DC and AC components, respectively. u and v represent the horizontal and vertical coordinates on the surface of fiber bundle. D means the domain of integration. Thus, the AC/DC ratio of the optical signal can be obtained as

$$\mathrm{AC/DC} = \frac{I_{\mathrm{AC}}}{I_{\mathrm{DC}}} = \frac{\max(I) - \min(I)}{\max(I) + \min(I)}. \tag{2}$$

Considering the angle θ between the reference and measurement beams, and the wavelength λ, the interference fringe period d in Fig. 1(b) can be expressed as

$$d = \frac{\lambda}{\sin\theta}. \tag{3}$$

Due to the bright and dark fringes in the domain D, as shown in Fig. 1(b), the light intensity of AC component after integration will reduce rapidly with the enlargement of angle θ between two interference beams. In the structure proposed, the fiber bundle without couplers is used to receive only part of the light in the interference area, as Fig. 1(b) shows. Owing to the small diameter of the fiber core, the integral effect is greatly weakened. The AC/DC ratio is able to keep within a high value and the nonlinearity of DWS detection is reduced within the larger angular measurement range despite of the interference fringes.

The structure described above can also be applied in other laser or grating interferometers as long as there is no corner cube in the optical structure that eliminates the angle between the interference beams caused by the target rotation. Along with the fiber bundle, the AC/DC ratio is greatly improved, which reduces the requirement for photodetectors. However, the power of AC component actually declines due to the reduced detection area, and a laser source with a larger output power and proper beam diameter would be one way to increase the signal power.

To explicate the working principle as well as the decoupled algorithm in DWS, the relation between the three DoFs of the target and the measurement phase in Eq. (4) is derived using the ray tracing method and kinematic analysis first [18,19]. In the equation,

$$\Delta\varphi = \frac{2\pi}{\lambda}\Delta L = f(\Delta\theta_x, \Delta\theta_y, \Delta z), \tag{4}$$

where $\Delta\phi, \Delta L$ represent the detected phase and the optical path length changes, respectively, $\Delta z, \Delta\theta_x, \Delta\theta_y$ are the linear and angular displacements of the target relative to the interferometer.

As shown in Fig. 2(a), the optical length of measurement wave can be divided into several parts. To explain the derivation, the ab part is taken as an example, and we make the center of the PBS as the origin of coordinate frame $\{A\}$. The coordinates of point a, $^A P_a$, can be expressed as $[0001]^T$, and similarly, the measurement wave vector, e_{ab}, as $[0010]^T$. The frame $\{B\}$ is established at the beam center on the target mirror. Thus, using the notations for Eq. (4), the homogeneous transformation matrix from frame $\{A\}$ to $\{B\}$ can be expressed as

$$^B_A T = \begin{bmatrix} \cos\Delta\theta_y & \sin\Delta\theta_x\sin\Delta\theta_y & \cos\Delta\theta_x\sin\Delta\theta_y & 0 \\ 0 & \cos\Delta\theta_x & -\sin\Delta\theta_x & 0 \\ -\sin\Delta\theta_y & \sin\Delta\theta_x\cos\Delta\theta_y & \cos\Delta\theta_x\cos\Delta\theta_y & \Delta z + l_{ab0} \\ 0 & 0 & 0 & 1 \end{bmatrix}, \tag{5}$$

where l_{ab0} is the initial distance between two coordinate frames in z direction. To obtain the optical length between PBS and M, l_{ab}, after the linear and angular displacements of the target, we express the coordinates of point b in frame $\{B\}$, $^B P_b$, as
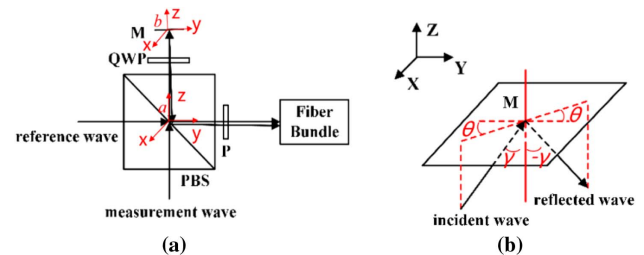

Fig. 2. (a) Coordinate definition of the ray tracing method and kinematic analysis (M: mirror, P: polarizer, PBS: polarize beam splitter, QWP: quarter wavelength plate). (b) The relation of the polar and azimuth angle between the incident and reflected wave.

$$^{B}P_{b} = {}^{B}_{A}T \times ({}^{A}P_{a} + l_{ab} \cdot e_{ab}) = \begin{bmatrix} {}^{B}x_{b} & {}^{B}y_{b} & {}^{B}z_{b} & 1 \end{bmatrix}^{T}. \tag{6}$$

So l_{ab} can be resolved by the prerequisite that the z coordinate of point b in frame $\{B\}$, ${}^{B}z_{b}$, equals zero. Moreover, based on the relation with the incident wave, the reflected wave vector can be described by the polar angle γ and azimuth angle θ, as Fig. 2(b) shows. Therefore, the practical optical length in each part of the measurement wave can be derived in sequence and phase changes can be expressed by

$$\Delta\varphi = \frac{2\pi}{\lambda} \sum_{i=ab,\,bc\ldots} (l_{i} - l_{i0}). \tag{7}$$

Considering the complexity of the formula derivation, numerical calculation is applied. For a three DoFs decoupled algorithm, results obtained above are fitted by a polynomial within the range of ± 600 µrad in rotation. To guarantee higher accuracy as much as possible, the quadratic term is adopted in the fitting process. After omitting high order fitting error, the phase changes $\Delta\varphi$ in each detection area can be expressed as

$$\begin{cases} \Delta\varphi_{1} = 2 \times \frac{2\pi}{\lambda}(-\Delta z - \alpha_{x} \cdot \Delta\theta_{x} - \alpha_{y} \cdot \Delta\theta_{y} + \beta \cdot (\Delta\theta_{x}^{2} + \Delta\theta_{y}^{2})) \\ \Delta\varphi_{2} = 2 \times \frac{2\pi}{\lambda}(-\Delta z + \alpha_{x} \cdot \Delta\theta_{x} - \alpha_{y} \cdot \Delta\theta_{y} + \beta \cdot (\Delta\theta_{x}^{2} + \Delta\theta_{y}^{2})) \\ \Delta\varphi_{3} = 2 \times \frac{2\pi}{\lambda}(-\Delta z + \alpha_{x} \cdot \Delta\theta_{x} + \alpha_{y} \cdot \Delta\theta_{y} + \beta \cdot (\Delta\theta_{x}^{2} + \Delta\theta_{y}^{2})) \\ \Delta\varphi_{4} = 2 \times \frac{2\pi}{\lambda}(-\Delta z - \alpha_{x} \cdot \Delta\theta_{x} + \alpha_{y} \cdot \Delta\theta_{y} + \beta \cdot (\Delta\theta_{x}^{2} + \Delta\theta_{y}^{2})) \end{cases}, \tag{8}$$

where, the subscripts 1–4 represent the fiber numbers in Fig. 1(b), and $\alpha_{x}, \alpha_{y}, \beta$ are the coefficients, which need calibration in consideration of beam and detector size, beam aberrations, alignment errors, and other factors. Hence, the three DoFs can be decoupled according to

$$\Delta\theta_{x} = \frac{\lambda}{4\pi} \frac{(\Delta\phi_{1} + \Delta\phi_{2}) - (\Delta\phi_{3} + \Delta\phi_{4})}{\alpha_{x}}, \tag{9}$$

$$\Delta\theta_{y} = \frac{\lambda}{4\pi} \frac{(\Delta\phi_{1} + \Delta\phi_{4}) - (\Delta\phi_{2} + \Delta\phi_{3})}{\alpha_{y}}, \tag{10}$$

$$\Delta z = \frac{\lambda}{4\pi} \left(\frac{(\Delta\varphi_{1} + \Delta\varphi_{2} + \Delta\varphi_{3} + \Delta\varphi_{4})}{4} - \beta \cdot (\Delta\theta_{x}^{2} + \Delta\theta_{y}^{2}) \right). \tag{11}$$

Compared to the decoupled algorithm of displacement in Eq. (11), it is clear that the tilt-to-length coupling caused by the target rotation is not taken into account in the conventional DWS algorithm shown as Eq. (12) [8,11]. And, this error aggravates as rotational angle increases, so

$$\Delta z \propto (\Delta\varphi_{1} + \Delta\varphi_{2} + \Delta\varphi_{3} + \Delta\varphi_{4}) \tag{12}$$

3. SIMULATIONS

To detail the DWS structure and method proposed, we make the simulations based on the ZEMAX ray tracing software that operates in a nonsequential mode. The simulation model in the software is shown in Fig. 3(a) and the optical layout is similar to the Michelson interferometer. The wavelength set in the model is 632.8 nm. The beam diameter is 4 mm and a detector is employed to get the interference light intensity and phase of each detection area. We set three DoFs displacement of the target by the interactive extension with MATLAB and a comparison ise made between the results of a 5 mm × 5 mm and a 0.2 mm × 0.2 mm detection area.

Figure 3(b) shows the interference pattern in the case of a 400 µrad angular displacement of the target. In a 5 mm × 5 mm detection area, all the interference fringes are received while only part of one fringe is received in a 0.2 mm × 0.2 mm detection area, effectively reducing the integral effect as well as the DC component, which is the reason for the high AC/DC ratio. The relation between the AC/DC ratio and the rotation of the target with a different detection area is shown in Fig. 3(c). The AC/DC ratio decreases quickly to 0 on the 5 mm × 5 mm detector as the target rotates. In contrast, the 0.2 mm × 0.2 mm detector can maintain the AC/DC ratio at a high level.

To illustrate the linear range of angular displacement in DWS, the measurement phase is obtained by the addition and subtraction of the phases on four detectors, according to Eqs. (9) and (10). As the measurement phase for the target rotation in Fig. 4(a) shows, under the condition of an angular displacement measurement error less than 1 µrad after linear
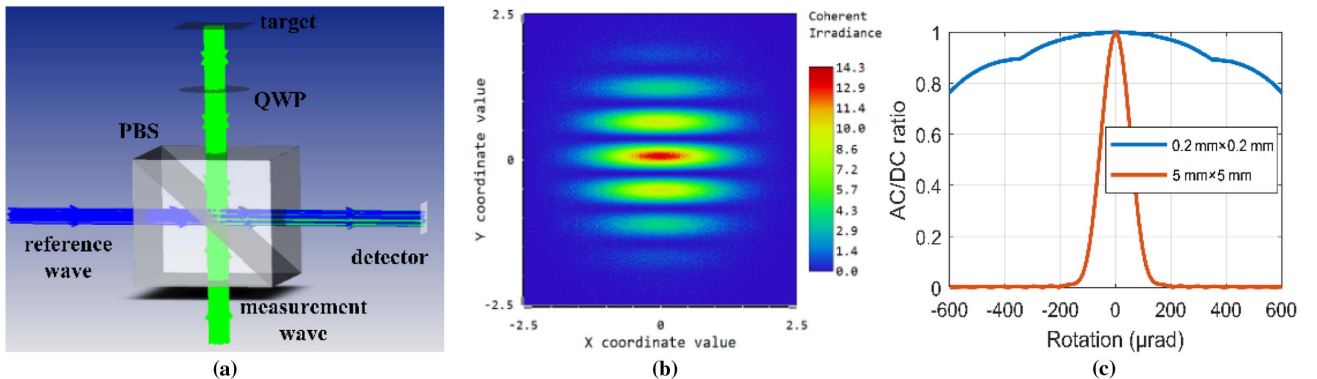

Fig. 3. (a) Simulation model in ZEMAX. (b) Interference pattern in the case of 400 µrad angular displacement of the target mirror. (c) The relation between the AC/DC ratio and the rotation of the target mirror with different detection areas.
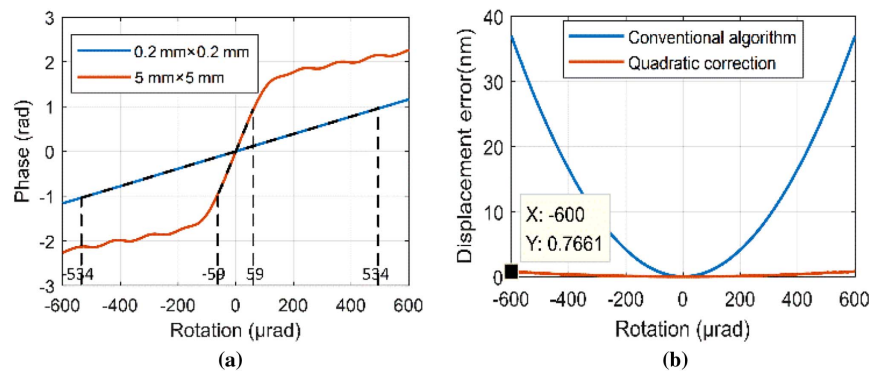
Fig. 4. (a) Measurement phase for the target rotation in DWS with different detection areas. (b) Displacement for the conventional algorithm and decoupled algorithm with quadratic correction.

fitting [12], the rotational measurement range increases from ± 59 to ± 534 µrad and the detection area decreases from 5 mm × 5 mm to 0.2 mm × 0.2 mm, which indicates that the linearity of the DWS detection is improved. As shown in Fig. 4(b), in the case of the target rotating, tilt-to-length coupling would result in a sub-nanometers error in the displacement measurement and can be ignored within a small rotational range. However, in a wide rotational range, tilt-to-length coupling would bring a tens-of-nanometer error and a conventional DWS algorithm for displacement measurement is not suitable, while it can be decreased to sub-nanometers employing the decoupled algorithm with a quadratic correction in Eq. (11).

4. EXPERIMENTS

The experimental configuration that compares the three DoFs laser interferometer based on DWS with a ZYGO commercial 3-axis position measurement interferometer (PMI) system (i.e., the contrast experiment device) is shown in Fig. 5.

In the experiment, a helium–neon (He–Ne) laser head producing two frequencies that are orthogonally linearly polarized was employed as the light source. The laser with diameter of 6 mm is split into two beams by the beam splitter (BS), one of which propagates into the three DoFs laser interferometer

based on DWS and the other propagates into the 3-axis PMI system. All of the measurement interference light is transmitted through the optical fibers and disposed in the same process system. The output power of the laser head is about 700 µW, with the 632.8 nm wavelength (model: ZMI 7702 Laser Head, ZYGO, Inc.). The displacement of the three DoFs is realized by a 6-axis precision piezo stage (model: P-587, PI, Inc.). The target is a hexahedron with reflective film, and it has high perpendicularity and parallelism to ensure two interferometers measure the same target motion without angular deviation. The three-axis laser interferometer (model: ZMI Compact 3-Axis HSPMI, ZYGO, Inc.) was employed to measure the same displacement of the three DoFs from the opposite ends. The phases of all the interference signals are extracted by the measurement board (model: ZMI 4100TM Series Measurement Board, ZYGO, Inc.). The other components, including the PBS, QWP, mirror, polarizer, and those optical mechanical components, are all from Thorlabs, Inc.

Figure 6 shows a character of the displacement measurement results with a stationary target in 10 s. From the amplitude spectral density and cumulative amplitude spectrum of the measurement results shown in Fig. 6, there is no other frequency difference except for natural frequency. In the high-frequency band, the noise level of the DWS readout is bigger, and the amplitude spectral density of the DWS is 10 pm/Hz$^{1/2}$ > 500 Hz and 2 pm/Hz$^{1/2}$ for ZYGO. The difference can be attributed the reduced total power received (i.e. sub-microwatt in each fiber), leading to a lower signal-to-noise ratio and higher electronic noise. While in the low frequency band, both are several nm/Hz$^{1/2}$, mainly caused by the environment. The standard deviation of the DWS with a fiber bundle is about 6.14 nm, achieving the same measurement level as 6.78 nm of ZYGO 3-axis PMI.

In the DWS structure proposed, the distance between two adjacent fibers decides the coefficient α in Eqs. (9) and (10), which has a great influence on the rotational measurement. According to previous works, the tilt measurement sensitivity increases with increasing detector dimension, but a larger detector size negatively influences the linear range in the DWS angular displacement measurement [10,12]. The sensitivity will increase with a larger distance and it is not consistent for the X and Y tilt, considering alignment and structure
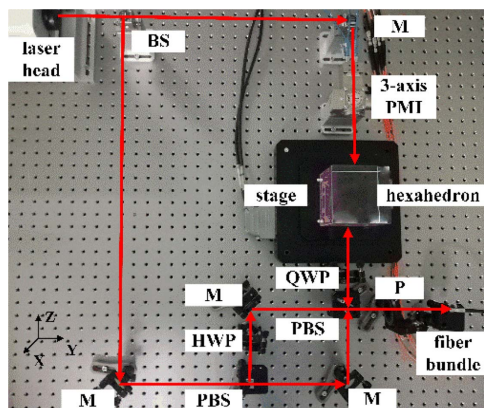

Fig. 5. Schematic of experimental setup comparing the three DoFs heterodyne laser interferometer with ZYGO PMI system. (BS: beam splitter, HWP: half wavelength plate, P: polarizer).
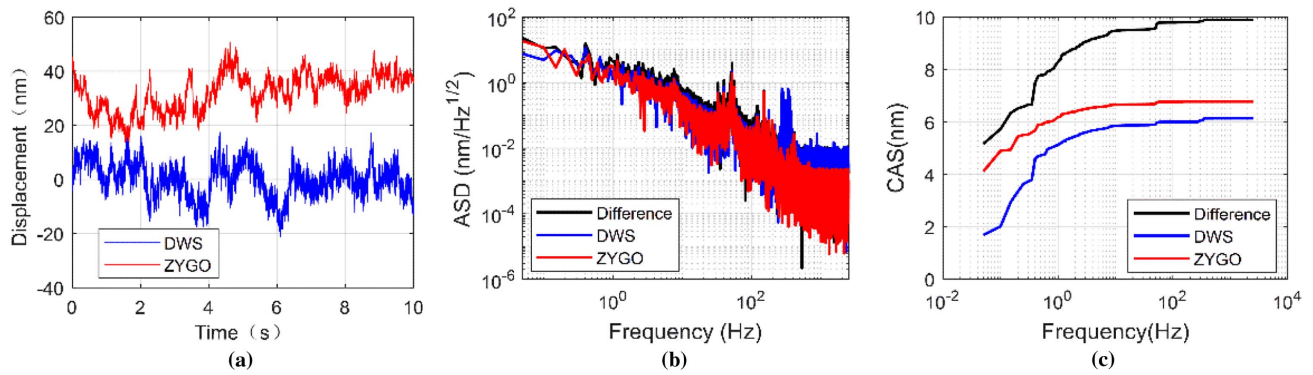
Fig. 6. (a) Measurement result of the object's displacement. Data axes have been offset for clarity. (b) The amplitude spectral density (ASD) of the measurement results. (c) The cumulative amplitude spectrum (CAS) of the measurement results.
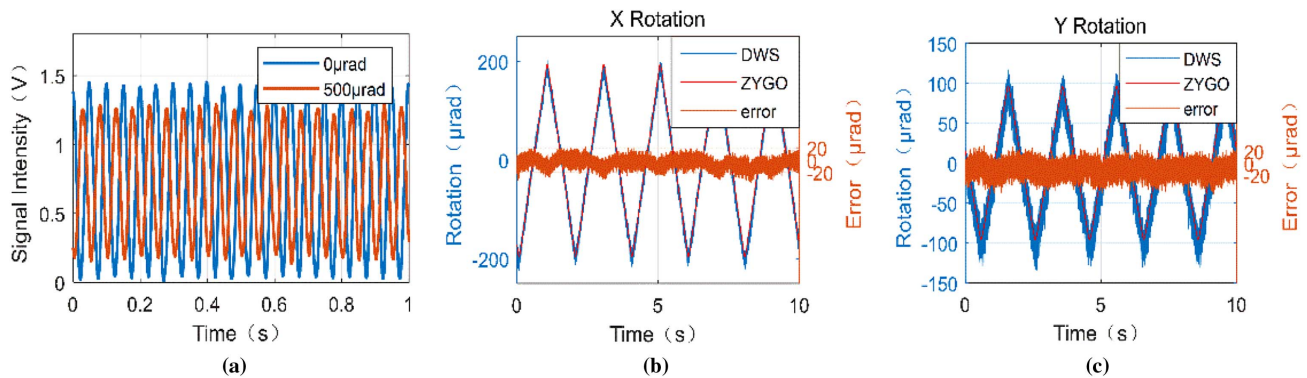

Fig. 7. (a) Waveform of the interference signals with rotation. (b) The measurement result of the object's rotation around the X axis. (c) The measurement result of the object's rotation around the Y axis.

parameter errors. When dividing by submillimeter-scale values of α, nanometer variation in the displacement measurement is amplified to microradians in rotational measurement (e.g. rotational measurement variation = 1 nm/0.25 mm = 4 µrad, assuming 1 nm for displacement measurement variation and 0.25 mm for the distance between two adjacent fibers).

Figure 7(a) shows the waveform of the interference signals with target rotation. The AC/DC ratio is $(1.42 – 0.06)/(1.42 + 0.06) = 92\%$ without rotation, which happens because the power of the two beams is not completely equal. And, the AC/DC ratio is about $(1.26 – 0.17)/(1.26 + 0.17) = 76\%$ with a 500 µrad rotation of the target, which agrees with the simulation results shown in Fig. 3(c). For angular displacement measurement, coefficients α_x and α_y in Eqs. (9) and (10) are calibrated at first through experiments, and the values are 0.292 mm and 0.233 mm, respectively. To verify the capacity of the new interferometer proposed, the stage is set to rotate around the X and Y axis simultaneously. The target moves periodically in the way of a ramp wave with a maximum angle of ± 200 µrad for the X axis and ± 100 µrad for the Y axis. According to the decoupled methods in Eqs. (9) and (10), the experimental results of the rotational measurement are shown in Figs. 7(b) and 7(c) using the coefficients calibrated. Compared to the ZYGO 3-axis PMI, the standard deviation

of the rotational measurement discrepancy is about 7.26 µrad in the X axis and 9.90 µrad in the Y axis. Considering the displacement measurement result of the DWS, the variation in the rotational measurement results in the experiment is reasonable.

5. CONCLUSION

We have realized and tested a three-DoF interferometer with DWS that can be used in wide range angular displacement measurement. The working principle for a high AC/DC ratio of the interference signals and a decoupled algorithm with quadratic tilt-to-length coupling correction in wide range angular displacement measurement are both explained in detail. The simulation and experimental results show that by applying a fiber bundle, the angular displacement measurement range of the interferometer increases to ± 534 µrad, expanded in the differential wavefront sensing.

REFERENCES

1. R. K. Heilmann, C. G. Chen, P. T. Konkola, and M. L. Schattenburg, "Dimensional metrology for nanometre-scale science and engineering: towards sub-nanometre accurate encoders," Nanotechnology **15**, S504–S511 (2004).

2. G. N. Peggs, A. J. Lewis, S. Oldfield, G. N. Peggs, A. J. Lewis, and S. Oldfield, "Design for a compact high-accuracy CMM," CIRP Ann **48**, 417–420 (1999).

3. G. Hechenblaikner, R. Gerndt, U. Johann, P. Luetzow-Wentzky, V. Wand, H. Audley, K. Danzmann, A. Garcia-Marin, G. Heinzel, M. Nofrarias, and F. Steier, "Coupling characterization and noise studies of the optical metrology system onboard the LISA Pathfinder mission," Appl. Opt. **49**, 5665–5677 (2010).

4. S. Thilo, G. Martin, W. Dennis, J. Ulrich, P. Achim, and B. Claus, "Picometer and nanoradian optical heterodyne interferometry for translation and tilt metrology of the LISA gravitational reference sensor," Classical Quantum Gravity **26**, 085008 (2009).

5. B. S. Sheard, G. Heinzel, K. Danzmann, D. A. Shaddock, W. M. Klipstein, and W. M. Folkner, "Intersatellite laser ranging instrument for the GRACE follow-on mission," J. Geodes. **86**, 1083–1095 (2012).

6. J. W. Kim, C.-S. Kang, J.-A. Kim, T. Eom, M. Cho, and H. J. Kong, "A compact system for simultaneous measurement of linear and angular displacements of nano-stages," Opt. Express **15**, 15759–15766 (2007).

7. S. R. Gillmer, R. C. G. Smith, S. C. Woody, and J. D. Ellis, "Compact fiber-coupled three degree-of-freedom displacement interferometry for nanopositioning stage calibration," Meas. Sci. Technol. **25**, 075205 (2014).

8. Y. Xiangzhi, S. R. Gillmer, and J. D. Ellis, "Beam geometry, alignment, and wavefront aberration effects on interferometric differential wavefront sensing," Meas. Sci. Technol. **26**, 125203 (2015).

9. G. Wanner, G. Heinzel, E. Kochkina, C. Mahrdt, B. S. Sheard, S. Schuster, and K. Danzmann, "Methods for simulating the readout of lengths and angles in laser interferometers with Gaussian beams," Opt. Commun. **285**, 4831–4839 (2012).

10. H.-Z. Duan, Y.-R. Liang, and H.-C. Yeh, "Analysis of non-linearity in differential wavefront sensing technique," Opt. Lett. **41**, 914–917 (2016).

11. X. Yu, S. Gillmer, S. C. Howard, S. Woody, and J. Ellis, "Compact six degree-of-freedom interferometer for precision linear stage metrology," in *30th American Society for Precision Engineering (ASPE) Annual meeting* (2015).

12. X. Yu, *Multi-Degree of Freedom Optical Metrology Techniques* (University of Rochester, 2017).

13. D. I. Robertson, E. D. Fitzsimons, C. J. Killow, M. Perreur-Lloyd, H. Ward, J. Bryant, A. M. Cruise, G. Dixon, D. Hoyland, D. Smith, and J. Bogenstahl, "Construction and testing of the optical bench for LISA Pathfinder," Classical Quantum Gravity **30**, 085006 (2013).

14. E. Morrison, B. J. Meers, D. I. Robertson, and H. Ward, "Experimental demonstration of an automatic alignment system for optical interferometers," Appl. Opt. **33**, 5037–5040 (1994).

15. E. Morrison, B. J. Meers, D. I. Robertson, and H. Ward, "Automatic alignment of optical interferometers," Appl. Opt. **33**, 5041–5049 (1994).

16. H. Müller, S.-W. Chiow, Q. Long, C. Vo, and S. Chu, "Active sub-Rayleigh alignment of parallel or antiparallel laser beams," Opt. Lett. **30**, 3323–3325 (2005).

17. S. Schuster, G. Wanner, M. Tröbs, and G. Heinzel, "Vanishing tilt-to-length coupling for a singular case in two-beam laser interferometers with Gaussian beams," Appl. Opt. **54**, 1010–1014 (2015).

18. C.-H. Liu and C.-H. Cheng, "Development of a grating based multi-degree-of-freedom laser linear encoder using diffracted light," Sens. Actuators A Phys. **181**, 87–93 (2012).

19. C. H. Liu, H. L. Huang, and H. W. Lee, "Five-degrees-of-freedom diffractive laser encoder," Appl. Opt. **48**, 2767–2777 (2009).